Mesoporous Tungsten Trioxide Photoanodes Modified with Nitrogen-Doped Carbon Quantum Dots for Enhanced Oxygen Evolution Photo-Reaction

Mabrook S. Amer [1], **Prabhakarn Arunachalam** [1], **Abdullah M. Al-Mayouf** [1], **Saradh Prasad** [2], **Matar N. Alshalwi** [1] **and Mohamed A. Ghanem** [1,*]

[1] Electrochemical Sciences Research Chair (ESRC), Chemistry Department, College of Science, King Saud University, Riyadh 11451, Saudi Arabia; msamer@ksu.edu.sa (M.S.A.); parunachalam@KSU.EDU.SA (P.A.); amayouf@ksu.edu.sa (A.M.A.-M.); malshalwi@KSU.EDU.SA (M.N.A.)

[2] Department of Astronomy and Physics, College of Science, King Saud University, Riyadh 11451, Saudi Arabia; sprasad@KSU.EDU.SA

[*] Correspondence: mghanem@ksu.edu.sa; Tel.: +966-114670405

check for updates

Abstract: Nanostructured photoanodes are attractive materials for hydrogen production via water photo-electrolysis process. This study focused on the incorporation of carbon quantum dots doped with nitrogen as a photosensitizer into *meso*porous tungsten trioxide photoanodes (N-CQD/*meso*-WO$_3$) using a surfactant self-assembly template approach. The crystal structure, composition, and morphology of pure and N-CQD- modified *meso*porous WO$_3$ photoanodes were investigated using scanning electron and transmission microscopy, X-ray diffraction, and X-ray photoelectron spectroscopy. Due to their high surface area, enhanced optical absorption, and charge-carrier separation and transfer, the resulting N-CQD/*meso*-WO$_3$ photoanodes exhibited a significantly enhanced photocurrent density of 1.45 mA cm^{-2} at 1.23 V vs. RHE under AM 1.5 G illumination in 0.5 M Na$_2$SO$_4$ without any co-catalysts or sacrificial reagent, which was about 2.23 times greater than its corresponding pure *meso*-WO$_3$. Moreover, the oxygen evolution onset potential of the N-CQD/*meso*-WO$_3$ photoanodes exhibited a negative shift of 95 mV, signifying that both the charge-carrier separation and transfer processes were promoted.

Keywords: *meso*porous; tungsten; trioxide; carbon; quantum; dots; photo-electrochemical; water splitting

1. Introduction

Photo-electrochemical (PEC) water splitting is a sustainable technology for the production of hydrogen fuel using water as the hydrogen source [1,2]. During the last decade, semiconductor metal oxide (SMO) photoelectrodes such as Fe$_2$O$_3$ [3], TiO$_2$ [4], ZnO [5], and BiVO$_4$ [6] have received considerable interest as favorable catalysts for converting solar energy into hydrogen fuel. Among them, tungsten trioxide (WO$_3$) is recognized as a favorable candidate for visible-light assisted water splitting due to its moderately narrow band energy gap (Eg = 2.6–2.8 eV), highly positive valence band energy levels for PEC water oxidation (3.0 V vs. RHE), and good stability against photo-corrosion [7,8]. SMO nanostructures with *meso*porous architectures are favorable for application as solar water splitting photoanodes because of their distinctive chemical and physical features [8,9]. In particular, their huge specific surface area delivers a higher density of available active sites as well as a greater light absorption depth, both of which lead to improved photocatalytic performance. The syntheses of ordered *meso*porous materials are classified as template-free or templating methods. Methods involving sol-gel [10], chemical vapor deposition (CVD) [11], and spray pyrolysis deposition [12]

mostly produce materials with irregular *meso*porous structures and disordered pore morphology. Besides, the hard-templating method produces organized *meso*porous materials with highly crystalline framework that replicates the structure of the *meso*porous SBA−15 silica, carbon, or cubic KIT-6 silica template [13,14]. However, this method has the disadvantages of being expensive and time-consuming and requires complex procedures. Therefore, it is not suitable for mass production applications. Synthetic methods using soft templates based on amphiphilic block copolymers or surfactants are another efficient and useful option for the preparation of *meso*structured materials with various morphologies and tunable pore architectures and can be used in large-scale production [15,16]. Triblock copolymer templates, such as Pluronic® F−127 and Pluronic® P123, are commonly employed for the fabrication of *meso*porous materials [17,18]. Unfortunately, these templates have a short segment chain length and low glass transition temperature (Tg), which results in the creation of *meso*porous materials with low crystallinity, amorphous or semi-crystalline channel walls, and uncontrollable pore size, which are not beneficial for solar water splitting devices [19–21].

Consequently, amphiphilic high molecular weight di-block copolymers, such as polyethylene oxide-b-polystyrene (PEO-b-PS), poly(methyl methacrylate) (PMMA), and poly(2-vinyl pyridine)-b-polystyrene (P2VP-b-PS), have recently been employed for the synthesis of *meso*porous SMOs [22,23]. In contrast to triblock copolymers, the di-block PEO-b-PS copolymer has the unique properties of strong hydrophobic/hydrophilic segments, a higher glass transition temperature, and abundant sp^2 hybridized carbon in the PS segments, which can be in situ converted into rigid amorphous carbon during the crystallization of the framework in an inert atmosphere. Thus, its ordered *meso*structured is retained when it is used as a template [23,24]. Moreover, to advance the PEC response of electrodes for water splitting applications, the precious metals loading Ag, Au, Pt, and Pd [25–27], as well as photosensitizers such as CdS [28], Bi2S3 [29], and CdSe [30], have been widely employed to modify SMO photoanode materials. However, these photosensitizer materials are unstable and are easily oxidized under the operating conditions of PEC anodes, which limit their potential usage in large-scale applications [31]. In contrast, the incorporation of carbon quantum dots (CQDs) and nitrogen-doped CQDs (N-CQDs) into SMO materials as a photosensitizer is considered to be promising, as carbon quantum dots are cost-effective, electrochemically stable, non-toxic, and composed of earth-abundant elements [32]. The CQDs can act as electron donors and acceptors, leading to the creation of hole/electron pairs and thus enhancing the light absorption and photocatalytic performance of the CQDs/SMO composites. Several reports of the incorporation of a CQD photosensitizer into SMOs to produce high-performance photocatalytic photoanodes have been published recently [33–35]. However, CQDs still have low photosensitization efficiency, which limits their utility for advanced practical applications. More recently, Lim and coworkers demonstrated that doping CQDs with heteroatoms such as nitrogen could significantly increase their light-harvesting, tuning band structure, and optical properties, and thus greatly enhance the PEC properties of hybrids, including the doped CQDs [36]. Zhao et al. demonstrated a facial self-assembly route to integrate ultra-small graphitic N-doped pencil nanodots (PND) into a highly ordered TiO_2 *meso*porous framework [37]. The hybrid catalyst showed high PEC activity and achieved a photocurrent density of ~1.73 mA cm^{-2} at 0.23 V vs. Ag/AgCl, which was 183 and 108% higher than that of the pure TiO_2 and undoped PND-TiO_2, respectively. The PEC performance was credited to the enhanced charge transfer rate between the TiO_2 frameworks and the modified PNDs through electron donation by the N atoms. Within this context, hybrid materials combining *meso*porous tungsten trioxide (*meso*-WO_3) and CQDs or N-CQDs have never been reported and could be a favorable candidate for promoting PEC performance for water oxidation. Herein, we reported a facile synthetic route for the fabrication of ordered *meso*-WO_3 via a dip-coating method and evaporation-induced self-assembly (EISA) using tetrahydrofuran (THF) as the solvent and PEO-b-PS as a template, followed by thermal treatment. The produced *meso*-WO_3 thin films were then decorated with various loadings of CQDs and N-CQDs via an impregnation method. The N-CQD/*meso*-WO_3 hybrid materials were systematically evaluated for their water oxidation activity under simulated light. Compared with the bare WO_3, the N-CQD/*meso*-WO_3 hybrid exhibited about

2.23 times higher oxygen evolution photocurrent density. The enhanced photocatalytic performance might be credited to the promoted photo-response range and highly efficient charge carrier separation.

2. Materials and Methods

2.1. Chemicals and Materials

Tungsten (VI), hexachloride (WCl$_6$ $\geq$ 99.9%), and tetrahydrofuran (THF, $\geq$99.5%) were acquired from Sigma Aldrich, Missouri, USA. The precursors used for the CQDs and N-CQDs were sucrose (C$_{12}$H$_{22}$O$_{11}$, $\geq$99.5%) and melamine (C$_3$H$_6$N$_6$, $\geq$99%), respectively, which were obtained from Aldrich, Missouri, USA. Sodium sulfate (Na$_2$SO$_4$, $\geq$99%), isopropanol (C$_3$H$_8$O, $\geq$99.5%), and acetone (C$_3$H$_6$O, $\geq$99.5%) were purchased from BDH Middle East, Dubai, UAE. The fluorine-doped tin oxide was used as the substrate (FTO, resistivity = 10^{-14} Ω·cm^{-2}, Lanbo Glass Ltd., Hong Kong, China). All reagents were used as received. Ultrapure water purification system of Milli-Q (Millipore, Inc., Darmstadt, Germany) was used to produce the deionized water with a resistivity of 18.2 MOhm cm.

2.2. Preparation of CQDs, N-CQDs, and Mesoporous WO$_3$ Hybrid Photoanodes

The N-doped CQDs were fabricated via a hydrothermal process using sucrose and melamine (C$_3$H$_6$N$_6$) as the sources for carbon and nitrogen, respectively. In a typical synthesis, 7 wt. % of melamine (0.0565 g) was dispersed in 30 mL of deionized water under ambient conditions and agitated vigorously using magnetic stirring for 1 h. Afterward, 0.75 g of sucrose was introduced to the previous transparent mixed solution at ambient temperature and stirred continuously for a further 30 min. Subsequently, the obtained solution was kept in a 40 mL Teflon-lined autoclave reactor and subjected to thermal heating for 5 h at 180 °C. Later, the products were collected, washed with water/ethanol, and then subjected to the drying process in an oven at 60 °C. Finally, the produced N-CQDs samples were denoted as N-CQD-x, where x represented the weight percentage of melamine used in the synthesis process (3, 5, 7, 13, or 20 wt. %). The CQDs were prepared using a procedure similar to that mentioned above but without melamine. The *meso*porous WO$_3$ (*meso*-WO$_3$) thin films were synthesized according to a self-assembly surfactant template and dip-coating method following the procedure reported by Li et al. [23]. An amphiphilic di-block copolymer with the composition PEO117-b-PS198 (Mn = 25850 g·mol^{-1}) was prepared using a previously reported procedure [23]. In a typical experiment, PEO117-b-PS198 (2.0 wt. %, 200 mg) was first dissolved in 10 g of THF, 0.6 g of concentrated HCl (37 wt. %) was carefully added slowly, and the subsequent mixture was magnetically stirred for 30 min. Afterward, WCl$_6$ (0.6 g) was introduced to the template mixture and agitated continuously for 2 h, after which the template mixture became highly viscous. Subsequently, the FTO substrates were pre-cleaned with a water-detergent mixture, isopropanol, and acetone, respectively, and then rinsed with deionized water. The obtained sol-gel solution was coated onto the FTO substrates using a dip-coating method (Xdip-MV1, West Bengal, India) with a 300 mm·min^{-1} withdrawal speed to obtain a transparent thin-film substrate as displayed in Figure S5. Afterward, the obtained film was rested horizontally at 25 °C for 20 min, dried at 40 °C for 24 h, and then annealed at 100 °C for 24 h to form the WO$_3$-surfactant templated films. Subsequently, the coating process was repeated until the desired number of layers (1–13 layers) of *meso*porous WO$_3$ had been applied. Afterward, the as-deposited films on the FTO substrate were pyrolyzed using a temperature ramp of 1 °C·min^{-1} to reach a final temperature of 350 °C for 3 h under a nitrogen atmosphere to decompose the surfactant. The films were cooled to temperature naturally and then annealed at 450 °C for another 1 h in the open air to form the *meso*porous WO$_3$ catalyst. To load different amounts of N-CQDs or CQDs, the *meso*-WO$_3$ thin films were immersed in 25 mL (1.5 mg·mL^{-1}) of a N-CQD or CQD solution for 1, 3, or 5 h. Lastly, the resulting N-CQD/or CQD/*meso*-WO$_3$ hybrids were rinsed with water, subjected to drying process at 70 °C for 6 h, and stored in a desiccator for further characterization.

2.3. Material Characterization

The crystallography and phase data of the fabricated *meso*-WO_3 samples were analyzed using powder X-ray diffraction (XRD, Rigaku Miniflex 600, Rigaku Corporation, Tokyo, Japan). The morphological structure of the fabricated *meso*-WO_3 catalysts was observed using field emission scanning electron microscopy (FE-SEM, JSM-7000F JEOL system, Tokyo, Japan) armed with energy dispersion X-ray spectroscopy (EDS, INCA 400 Oxford, High Wycombe, UK). The *meso*porous and fine structure of the hybrids were further examined using high-resolution transmission electron microscopy (HRTEM, JEOL 2100 F, FEI Tecnai G2 F30, Tokyo, Japan). The samples were characterized using Fourier-transform infrared spectroscopy (FTIR, Perkin Elmer GX spectrophotometer, Ohio, USA) and X-ray photoelectron spectroscopy (XPS, Specs SAGE 150, Thermo Fisher Scientific, MA, USA), and room-temperature photoluminescence (PL) spectra were obtained using a spectrofluorophotometer (Perkin Elmer LS55, Ohio, USA). The optical natures of the fabricated catalysts were assessed using a UV-vis-NIR spectrophotometer (Shimadzu UV-2600, MD, USA). The thickness of the composite films was assessed using a Bruker Dektak XT profilemeter (Coventry, UK). Nitrogen adsorption isotherms were obtained by means of NOVA 2200e surface area analyzer (Quantachrome Instruments, Florida, USA).

2.4. Photoelectrochemical Measurements of the Hybrid Materials

The PEC characterizations were evaluated through the potentiostat (BioLogic SAS, VSP-0478, Paris, France) electrochemical system in a three-electrode glass cell with a quartz window in 0.5 M Na_2SO_4 electrolyte solution (pH ~6.8). The modified *meso*-WO_3 deposited on the FTO photoanodes was employed as the working electrode, and the saturated calomel electrode (SCE) and Pt-mesh (0.5 × 1.0 cm^2) were employed as the reference and counter electrode, correspondingly. The potential was normalized to the reference hydrogen electrode (RHE) using the equation, $E_{RHE} = E_{SCE} + 0.244 V + 0.059 pH$ at 25 °C, where pH = 14 for 1.0 M KOH solution. Linear sweep voltammograms (LSV) were evaluated in the anodic direction in the dark and under illumination. A xenon lamp (300 W, HAL-320, JAPAN) provided with a solar spectrum of air mass 1.5 global (AM 1.5 G) irradiance. AM 1.5 G filter (was engaged as the light source. A Mott-Schottky (M-S) plot was acquired at a frequency of 1 kHz in the dark using an electrochemical impedance analyzer (BioLogic SAS, VSP-0478). Electrochemical impedance spectroscopy (EIS) analysis was performed in the dark and under illumination at an applied bias of 1.0 V vs. SCE.

3. Results and Discussion

3.1. Characterization of the CQDs and N-CQDs

The size and microstructure of the as-prepared N-CQDs were investigated using transmission electron microscope (TEM). The TEM micrograph in Figure 1 shows that the N-CQDs were highly dispersed, with a size distribution of 2 to 7 nm and an average particle size of 4 nm, as shown in the inset particle size histogram. The HRTEM image of a single N-CQD (inset in Figure 1) clearly shows that the as-synthesized N-CQDs exhibited a lattice spacing of 0.21 nm, which corresponds to the d-spacing of the (100) crystal plane of graphite [38]. The surface chemistry and functional groups of the fabricated CQDs and N-CQDs were investigated using FTIR spectroscopy. The FTIR spectra, displayed in Figure S1, reveal that all the CQD and N-CQD samples exhibited a broad peak in the range 3100–3500 cm^{-1}, which showed the existence of O–H and NH_2 stretching vibrations [38,39]. The peaks at around 2925 cm^{-1} were credited to the CH_3 and CH_2 stretching modes, while the peak at 1705 cm^{-1} was ascribed to C=O stretching vibrations, likely associated with the existence of carboxylic acid or amide groups [38,40]. The peaks at 1616 cm^{-1} were assigned to the N-H bending vibration, while the peak at 1445 cm^{-1} corresponded to C–N vibrations [40]. Moreover, the bending vibrations of the C–O bond and the stretching vibrations peak of the C–O–C bond were observed at 1388 and 1027 cm^{-1}, respectively [41]. Interestingly, as the nitrogen precursor (melamine) content was increased from 7 to

20%, the intensity of the N–H and C–N peaks at 1616 cm^{-1} and 1445 cm^{-1} was enhanced, while the opposite trend was observed for the C=O peak at 1705 cm^{-1}. This suggests that as the nitrogen content of the N-CQDs was increased, a concurrent decrease in the oxygen content was observed.
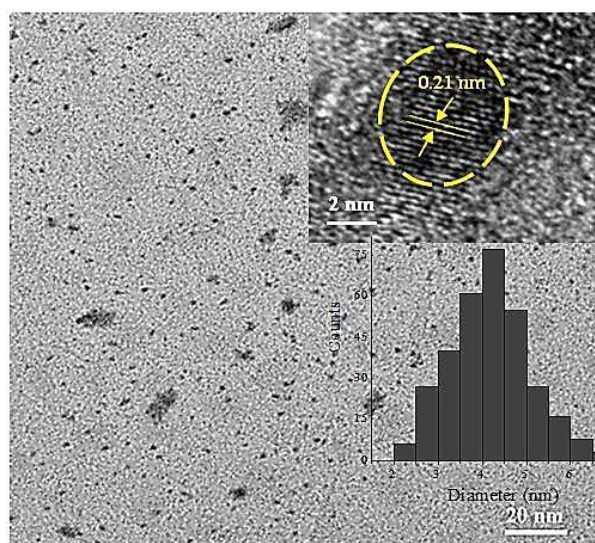
Figure 1. Transmission electron microscopy (TEM) image of the fabricated N-doped carbon quantum dots (7-N-CQDs), insets are the high-resolution TEM (HRTEM) image and its corresponding particle-size distribution histogram of 7-N-CQDs.

The XPS study was carried out to assess the surface states and composition of the CQD and N-CQD samples. As shown in Figure S2a and by comparison to the CQD spectrum, the XPS survey spectrum for N-CQD-7 and N-CQD-20 contains C, N, and O peaks at binding energies of 285, 400, and 531 eV, respectively. The XPS spectra revealed that the elemental composition of N-CQD-20 was carbon (52.3%), nitrogen (20.97%), and oxygen (26.73%). These values were very close to those obtained from the EDX elemental analysis displayed in Figure S3. The high-resolution C 1s spectrum of the N-CQD sample displayed in Figure S2b exhibits four main peaks. The peak noticed at 284.05 eV was attributed to the C–C bonds of the graphitic structure, suggesting that the graphite structure predominated in the N-CQD sample. The peaks at 286.88, 290.23, and 293.24 eV can be allocated to carbon in the form of C–N, C–O (sp3), and C=O, correspondingly [42]. Deconvolution of the N 1s core spectrum in Figure S2c revealed two main peaks centered at 398.77 and 401.98 eV, confirming the presence of nitrogen atoms in pyrrolic- and graphitic-like C–N–C (sp3) and (C)3–N (sp3) structures, correspondingly [42,43]. The O 1s core spectrum of N-CQD-7 in Figure S2d might be deconvoluted into two main peaks at 530.1 eV and 532.80 eV, indicating the existence of C=O and C–OH or C–O–C, respectively [43]. The FTIR and XPS results indicate that the surfaces of the fabricated N-CQDs were functionalized with multiple oxygen and nitrogen groups. More importantly, the data described above confirmed that melamine successfully served as a nitrogen source during the hydrothermal synthetic route of the N-CQDs.

The optical nature of the CQD and N-CQD samples was examined using UV-Vis absorbance and PL spectroscopy as illustrated in Figure S4. UV-Vis spectra of the CQDs and N-CQDs dispersed in water are displayed in Figure S4a. The N-CQDs exhibited a strong UV-vis absorption peak at around 335 nm. This peak originated from the aromatic n-π* transition of the C=O, C–N, or –C–OH bonds, which may be from hydroxyl (–COOH) or amine (–NH$_2$) groups on the surface of the N-CQDs [44]. The inset in Figure S4a shows that the N-CQD dispersion was transparent with a faint yellow color, while under a UV excitation wavelength of 365 nm, it exhibited blue fluorescence, demonstrating the bright luminescence of the prepared N-CQDs. This observation clearly indicated that the N-CQDs had different UV absorption and fluorescence emission behavior than the undoped CQDs. The PL emission spectra of the CQDs, N-CQD-7, and N-CQD-20 in the excitation wavelength range from 340 nm to 540

nm, as displayed in Figure S4b–d, respectively. The spectrum of the diluted N-CQD dispersion was dependent on the excitation wavelength, and the emission peaks varied from 440 to 525 nm under an excitation of 350–540 nm. Furthermore, not only was the fluorescence emission of the prepared N-CQDs stronger than that of the CQD solution of the same concentration, but the maximum fluorescence emission wavelength (λ_{em}) was also blue-shifted, as displayed in Figure S4c. The fluorescence emission intensity of N-CQD-7 was 9.7 times stronger than that of CQD, which could be explained by a reduction in the number of non-radiative recombination centers on the N-CQD surface [44]. Interestingly, the PL intensity of the N-CQDs under UV excitation improved considerably as the N doping level was increased, as shown in Figure S4e. The N-CQDs with 7% N displayed the uppermost PL intensity among all the samples. In particular, the strongest emission band was positioned at 533.4 nm under 480 nm excitation. Further, the PL emission of the N-CQDs shifted to higher wavelength as its intensity increased. This behavior was attributed to the surface defect emission derived from the CQDs and was inconsistent with previous reports in the literature [45]. The external quantum yields (EQY) of the N-CQDs under 360 nm excitation were assessed using quinine sulfate (QS) as the calibration standard sample. As displayed in Figure S4e, N-CQD-7 revealed a greater EQY of 74.3%, which was superior to that of N-CQD-20 (60.4%), N-CQD−13 (33.2%), N-CQD-5 (18.4%), and N-CQD-3 (13.4%). This high PL EQY was mostly due to the attendance of O and N atoms. In particular, the heteroatoms in the CQD lattice could reduce the π-connections between the sp^2-domains of carbon atoms, changing their electronic structure and thus suppressing non-radiative energy dissipation [42]. Significantly, increasing the N-doping level in the N-CQDs increased the photoexcitation efficiency, that is, fewer photo-induced electrons in the N-CQDs were quenched by energy traps. Thus, among the various N-CQDs studied, N-CQD-7 exhibited the best photosensitization performance for PEC applications. Thus, CQDs and N-CQD-7 were combined with the *meso*-WO$_3$ photoanodes as photosensitizers for PEC water oxidation.

3.2. Characterization of Meso-WO$_3$ and the CQD/Meso-WO$_3$ and N-CQD/Meso-WO$_3$ Hybrids

The morphology and *meso*structure of the *meso*porous tungsten trioxide modified with N-CQDs were examined using field emission scanning electron microscopy (FESEM) and HRTEM. The FESEM images of the attained *meso*-WO$_3$ electrodes are displayed in Figure 2. In particular, the *meso*-WO$_3$ catalyst annealed at 350 °C in N$_2$ for 3 h (see Figure 2a) and then at 450 °C in air for 1 h (see Figure 2b) clearly exhibited a well-defined and interconnected *meso*porous framework that extended over a very large domain. The FESEM images revealed that the *meso*porous morphology of the catalyst did not change during annealing in N$_2$ and air, which confirmed the successful creation of the WO$_3$ *meso*porous structure. This can be explained by the fact that the residual carbon can maintain the tungsten oxide *meso*structures and prevent wall expansion during annealing in air after burning the surfactant in an N$_2$ atmosphere.

The residual carbon was then removed after annealing in air, leaving the high-surface-area WO$_3$ *meso*porous structure. However, as shown in Figure 2c, direct one-step annealing in air at 450 °C for 2 h led to the destruction of the *meso*structures and the formation of adjoining WO$_3$ particles with a mean particle size of 40 nm. One-step direct calcination in the air caused the concurrent removal of carbon and WO$_3$ nanoparticle growth, which destroyed the *meso*porous structure. The FESEM image of the WO$_3$, fabricated in the absence of a surfactant (*bulk*-WO$_3$) in Figure 2d, does not exhibit any obvious pores, and the surface morphology of the *bulk*-WO$_3$ consisted of an aggregated nanoparticle structure with a mean particle size of 20 nm. It worth noting that the surface area of the *bulk*-WO$_3$ was 18 m$^2\cdot$g^{-1}, which was significantly less than that of *meso*-WO$_3$, as confirmed by the sorption isotherm results shown below.

Figure 3 displays the HRTEM images of the *meso*-WO$_3$ and the modified N-CQD-7/*meso*-WO$_3$ catalysts. The HRTEM image displayed in Figure 3a reveals that the fine structure of the *meso*-WO$_3$ catalyst exhibited distinct *meso*pores arranged in a highly ordered 2D hexagonal *meso*structure, with an average pore size of ~5 nm. Furthermore, the higher resolution TEM image in Figure 3b displays that

the *meso*-WO$_3$ framework consisted of well-crystallized walls with a lattice spacing of 0.265 nm and 0.382 nm, corresponding to the (200) and (020) diffraction planes of WO$_3$ (JCPDS # 43–1305).
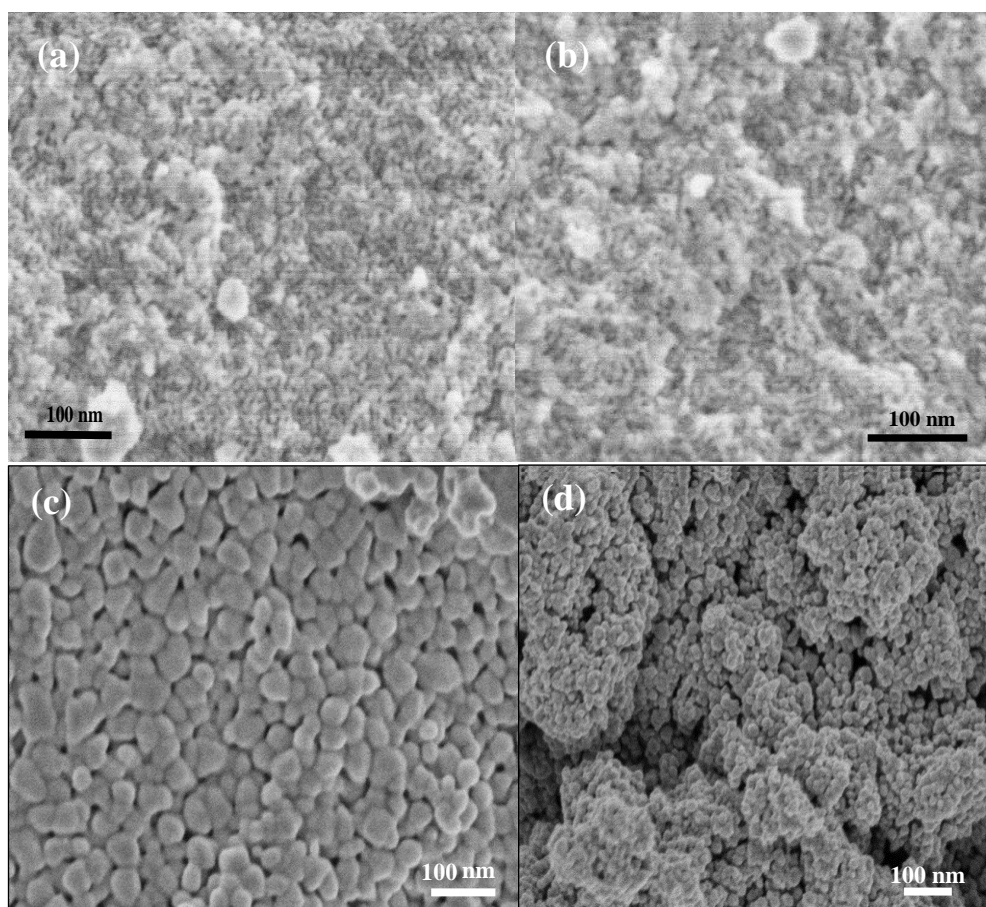
Figure 2. Field emission scanning electron (FESEM) images of (**a**) *meso*-WO$_3$ catalyst after annealed at 350 °C in the N$_2$ atmosphere for 3 h (**b**) *meso*-WO$_3$ catalyst after the second step of annealing in air at 450 °C for 1 h. (**c**) WO$_3$ annealed in one step at 450 °C in air (**d**) *bulk*-WO$_3$ prepared under similar condition but in absence of PEO-PS template.

Figure 3c shows the TEM image of the modified N-CQD-7/*meso*-WO$_3$ catalyst. The N-CQDs (dark spots) were attached to the surface of *meso*-WO$_3$ (yellow circles) and the *meso*structures of the *meso*-WO$_3$ substrate remained unchanged, demonstrating the successful loading of the N-CQDs on the surface of *meso*-WO$_3$. The HRTEM image in Figure 3d evidently shows the (100) and (020) lattice fringes with a spacing of 0.21 and 0.382 nm, agreeing to the N-CQDs and WO$_3$, respectively. Figure 4a reveals the N$_2$ sorption isotherms of the *meso*-WO$_3$ electrodes annealed under different annealing conditions, which exhibited type-IV curves with an H$_2$-type hysteresis loop. For the *meso*-WO$_3$ sample, the distinct capillary condensation step at a relative pressure of P/Po ~0.45 to 0.80 indicated the uniform *meso*porosity of the material. Another sharp N$_2$ uptake with an H$_2$-hysteresis loop at a higher relative pressure of P/P0 > 0.85 reflected the structural defects formed via pyrolysis. In contrast, the *bulk*-WO$_3$ showed typical sorption isotherms resulting from the aggregation of the nanoparticles. Figure 4b shows the pore size distributions of the *meso*-WO$_3$ electrodes calculated from the adsorption branch via Barrett-Joyner-Halenda (BJH) method, in which a uniform pore size of around 5 nm was observed. The detail of the textural properties of the *meso*-WO$_3$ and *bulk*-WO$_3$ are reported in Table S1. Clearly, the calculated Brunauer-Emmett-Teller (BET) surface area of the *meso*-WO$_3$ was 105 m$^2 \cdot$g^{-1}, which was higher than that obtained for *bulk*-WO$_3$ (18 m$^2 \cdot$g^{-1}) and *meso*-WO$_3$ directly annealed in air at 450 °C (28 m$^2 \cdot$g^{-1}). Moreover, the high surface area, open porous structure, and uniform pore size of the

meso-WO$_3$ materials can be exploited for loading co-catalysts onto their surfaces, making them an ideal electrode material for various energy-related applications such as water splitting devices, solar cells, and batteries.
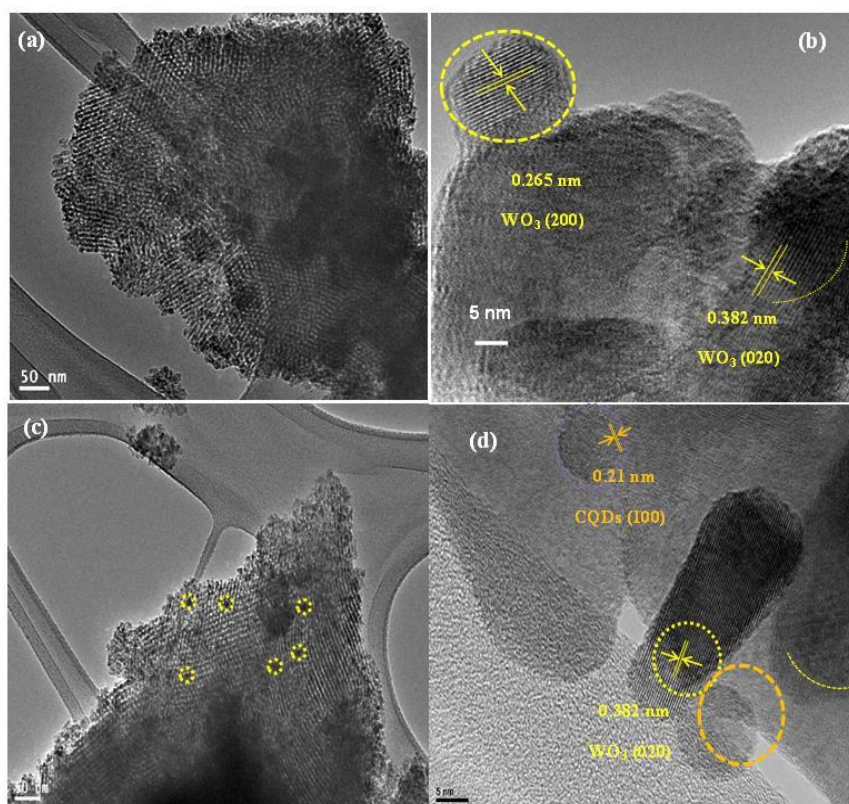
Figure 3. HRTEM images of (**a**) *meso*-WO$_3$ (**b**) 7-N-CQDs/*meso*-WO$_3$ sample, and a higher magnified HRTEM images of (**c**) *meso*-WO$_3$, (**d**) 7-N-CQDs/*meso*-WO$_3$ after annealing at 350 °C in N$_2$ and 450 °C in air.
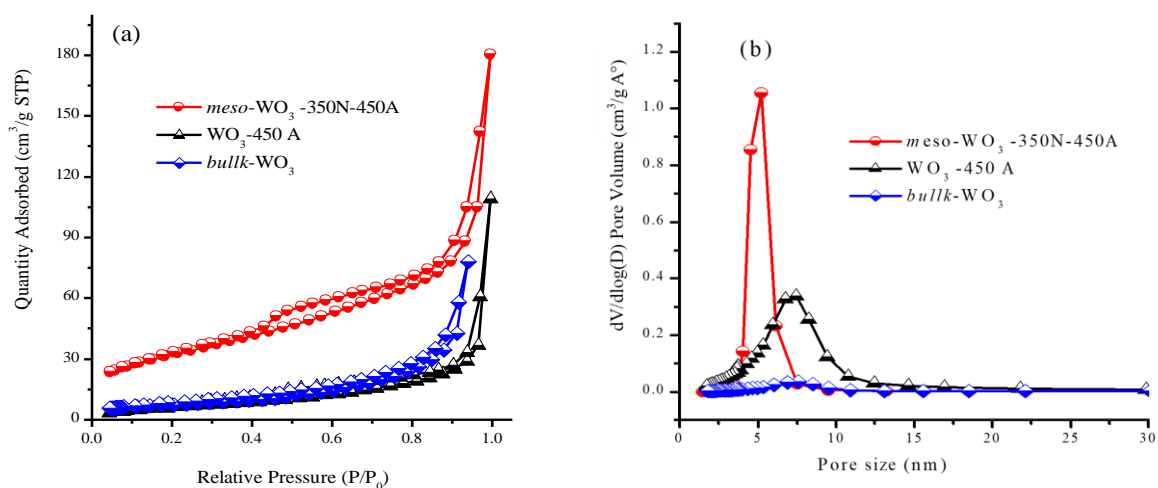
Figure 4. (**a**) N2 sorption isotherms and (**b**) Barrett, Joyner, and Halenda (BJH) pore size distributions of *meso*-WO$_3$ and *bulk*-WO$_3$ samples.

As displayed in Figure S5, the *meso*-WO$_3$ photoanodes were modified with CQD and N-CQD by dipping the *meso*-WO$_3$/FTO photoanodes in the CQD solutions for different lengths of time after the annealing steps. The *meso*-WO$_3$/FTO showed a light red color after being dipped in the CQD solution for 5 h, indicating the successful deposition of the CQDs onto the surface of WO$_3$ (Figure S5, SI).

Figure 5 reveals the diffraction patterns of the pure *meso*-WO$_3$, CQD/*meso*-WO$_3$, and N-CQD/*meso*-WO$_3$ photoanodes. The diffraction peaks of pure *meso*-WO$_3$ might be well-indexed to the planes of monoclinic WO$_3$ (JCPDS No.01-072-0677), confirming the successful synthesis of *meso*-WO$_3$. The XRD peaks of CQD/*meso*-WO$_3$ and N-CQD/*meso*-WO$_3$ were consistent with those of pure *meso*-WO$_3$, indicating that the addition of the N-CQDs did not alter the crystalline phase of *meso*-WO$_3$. The XRD peaks of the CQDs and N-CQDs could not be resolved in the CQD/*meso*-WO$_3$ and N-CQD/*meso*-WO$_3$ composites, possibly due to the low loading amount and dispersion of the CQDs, which was consistent with the literature [42].
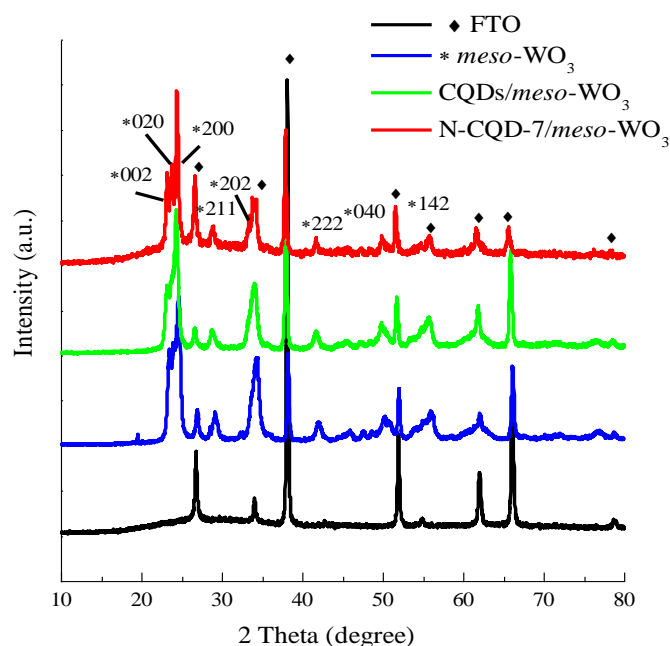
Figure 5. XRD patterns of *meso*-WO$_3$, CQDs/*meso*-WO$_3$ and N-doped CQDs/*meso*-WO$_3$ composites.

The N-CQD-7/*meso*-WO$_3$ electrode was examined using XPS analysis as displayed in Figure 6. The XPS wide survey spectrum of N-CQD/*meso*-WO$_3$ in Figure 6a indicated the attendance of the elements W, O, C, and N at the surface of the photoanode. In Figure 6b, the core spectrum of W 4f shows two well-resolved peaks at 36.25 and 38.40 eV, which were assigned to the W 4f$_{7/2}$ and W 2f$_{3/2}$ orbital signals. Moreover, the narrow O 1s peak in Figure 6c can be deconvoluted to three peaks appearing at binding energies of 528.77, 530.90, and 531.61 eV, corresponding to the lattice oxygen of the layer-structured WO$_3$ and adsorbed H$_2$O or surface hydroxyl oxygen, correspondingly [15]. The C 1s high-resolution spectrum in Figure 6d contains three different contributions at 284.90, 286.28, and 288.63 eV, which were related to carbon in the C–C, C–O, and C=N/C=O states, respectively [15–42]. The high-resolution N 1s spectrum in Figure 6e exhibits two peaks centered at 398.70 and 402.0 eV, which were credited to the C–N–C and (C)$_3$–N bonds [43,44], confirming that the surface of the N-CQD/*meso*-WO$_3$ was rich in nitrogen-containing functional groups. Thus, the C 1s, O 1s, and N 1s spectra further demonstrated that the N-CQDs were loaded to the surface of the *meso*-WO$_3$ substrate and that the N-CQD/*meso*-WO$_3$ composites had successfully been fabricated.
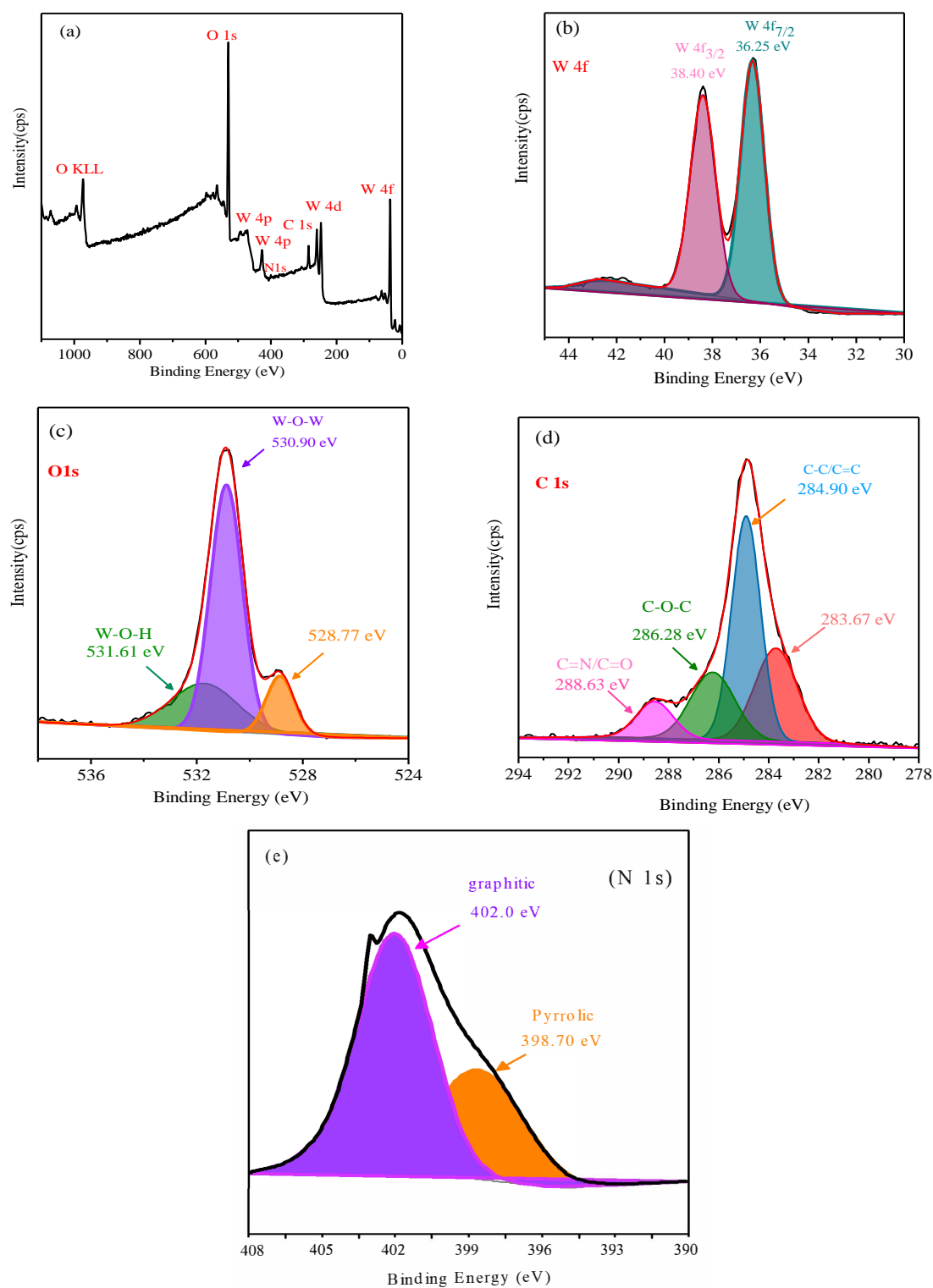
Figure 6. XPS spectra of as-synthesized N-CQDs/*meso*-WO₃ composite, (**a**) survey, (**b**) W 4f, (**c**) O 1S, (**d**) C 1s, and (**e**) N 1s core spectrum.

To examine the effect of the CQD and N-CQD doping on the light-harvesting capability of *meso*-WO₃, the optical properties of *meso*-WO₃ and the CQD and N-CQD/*meso*-WO₃ photoanodes were investigated using UV–vis absorption. As depicted in Figure 7a, the *meso*-WO₃ photoanodes exhibited optical absorption in the range of 300–473 nm, and the absorption spectrum capacity in the visible-light region was significantly enriched by the addition of N-CQDs. Figure 7b displays the Tauc plots of

the *meso*-WO$_3$ and N-CQD/*meso*-WO$_3$ composite films. The band gaps of the composite films were evaluated by plotting $(\alpha h\nu)1/2$ against the photon energy [46]. The plot of $(\alpha h\nu)1/2$ vs. the photon energy (hν), displayed in Figure 7b, was used to evaluate the bandgap energies of the *meso*-WO3 and N-CQD-7/*meso*-WO$_3$ photoanodes. The bandgap of the pristine *meso*-WO$_3$ photoanode was around 2.70 eV, while that of the N-CQD-7/*meso*-WO$_3$ photoanode was 2.63 eV. Moreover, the conduction band (CB) and valence band (VB) of the *meso*-WO$_3$ and N-CQD-7/*meso*-WO$_3$ photoanodes were assessed using the following equation [47]:

$$E_{CB} = \chi - E_e + 0.5\,E_g; E_{VB} = E_{CB} + E_g \tag{1}$$

where χ represents the absolute electronegativity of the semiconductor, with the χ value of WO$_3$ being 6.59 eV [48]; E_e is the energy of free electrons on the hydrogen scale (about 4.5 eV). Thus, the E_{CB} and E_{VB} of WO$_3$ were assessed to be +0.74 eV and +3.44 eV for *meso*-WO$_3$ respectively.
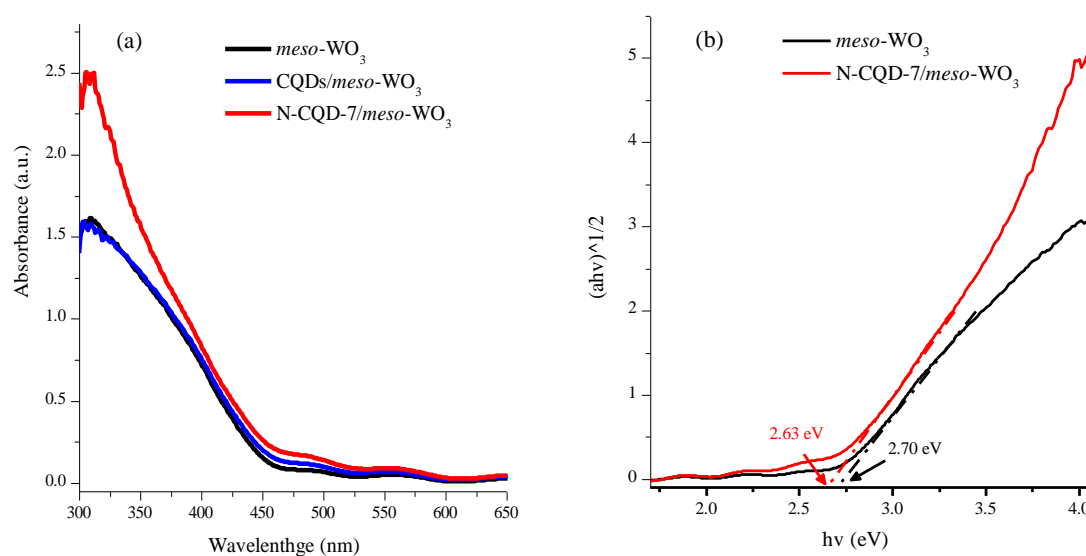
Figure 7. (**a**) UV-vis absorption of pristine *meso*-WO$_3$, CQDs/*meso*-WO$_3$, and N-CQDs/*meso*-WO$_3$ photoanodes; (**b**) Tauc plots of the *meso*-WO$_3$, and N-CQDs/*meso*-WO$_3$ photoanodes.

3.3. Photo-Electrochemical Properties of the Meso-WO$_3$ Photoanodes

The PEC activities of the as-synthesized *meso*-WO$_3$, CQD/*meso*-WO$_3$, and N-CQD-7/*meso*-WO$_3$ photoanodes toward water oxidation were investigated in the dark and under visible-light irradiation in a 0.5 M Na$_2$SO$_4$ solution (pH ~6.8) without adding a sacrificial agent or co-catalyst. Beforehand, the photocurrent of the *meso*-WO$_3$ photoanode was optimized by varying the film thickness, which was measured by profilometer as displayed in Figure S6. Figure 8a displays the photocurrents obtained (at 1.23 V vs. RHE) using *meso*-WO$_3$ photoanodes fabricated with various thicknesses as examined using chopped cyclic voltammograms under 100 mW·cm^{-2} visible-light excitation. As shown, the photocurrent increased from 0.21 to 0.58 mA·cm^{-2} as the thickness of the *meso*-WO$_3$ film was increased from 250 nm to 1.42 μm due to promoted light absorption, and consequently, enhanced hole-electron pair photo-generation.
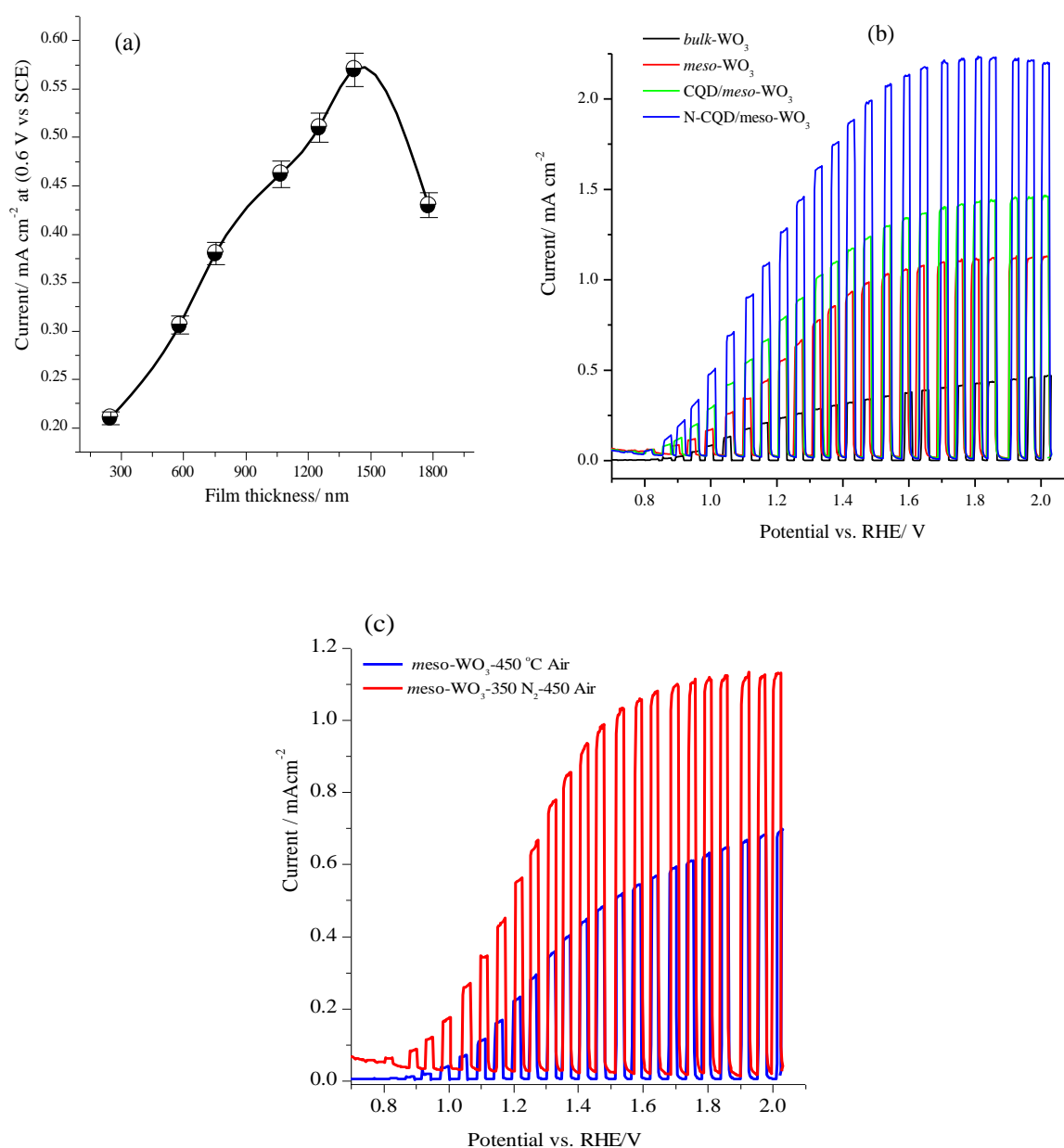
Figure 8. (**a**) Plot for the photocurrent obtained (at 1.23 V vs. RHE) using *meso*-WO$_3$ photoanodes fabricated with various thicknesses, (**b**) chopped cyclic voltammograms for *meso*-WO$_3$, CQDs/*meso*-WO$_3$, and N-CQDs/*meso*-WO$_3$ in 0.5 M Na$_2$SO$_4$ under visible-light excitations, (**c**) chopped cyclic voltammograms in 0.5 M Na$_2$SO$_4$ under irradiation for *meso*-WO$_3$ photoanodes thermally annealed at 450 °C and 350 N$_2$ and directly annealed in air at 450 °C upon visible illumination.

However, the photocurrent decreased when the thickness of the *meso*-WO$_3$ reached about 1.78 μm due to an increase of the charge recombination rate. Thus, the optimum photocurrent of 0.58 mA·cm^{-2} was achieved at a film thickness of 1.42 μm and 1.23 V vs. RHE under standard conditions. These results are comparable with those previously published for *meso*porous WO$_3$-based materials [7,49]. In addition to the film thickness, the surface film morphology and nanoarchitecture also influenced the PEC performance of the semiconductor photoanodes. Figure 8b shows the chopped LSVs of the *bulk*-WO$_3$, *meso*-WO$_3$, CQD/*meso*-WO$_3$, and N-CQD-7/*meso*-WO$_3$ photoanodes (film thickness about 1.4 μm) at 50 mV·s^{-1} under pulsed light irradiation in 0.5 M Na$_2$SO$_4$ solution (pH ~6.8). Upon illumination, the photocurrent of the photoanodes at 1.23 V vs. RHE decreased in the order N-CQD-7/*meso*-WO$_3$ (1.45 mA·cm^{-2}) > CQD/*meso*-WO$_3$ (0.8 mA·cm^{-2}) > *meso*-WO$_3$ (0.65 mA·cm^{-2}) > *bulk*-WO$_3$ (0.25 mA·cm^{-2}).

The *meso*-WO$_3$ electrode exhibited a photocurrent density of 2.6 times greater than that of its corresponding *bulk*-WO$_3$ electrode, which was credited to the greater number of active sites (higher surface area) of the *meso*-WO$_3$ photoanodes exposed to the electrolyte, which enhanced the PEC activity. Furthermore, the N-CQD-7/*meso*-WO$_3$ photoanodes demonstrated a significantly higher photocurrent density of 1.45 mA·cm^{-2}, which was 1.8 and 2.23 times greater than that of the CQDs/*meso*-WO$_3$ and bare *meso*-WO$_3$, respectively. Therefore, the photocurrent properties of the pristine *meso*-WO$_3$ were remarkably improved by modification with N-CQDs, which suggested that the N-doped CQDs dramatically improved the charge transfer between the CQDs and the *meso*-WO$_3$ thin film via electron donation from the introduced N-atoms. As presented in Table S1, the photocurrent density of 1.45 mA·cm^{-2} at 1.23 V vs. RHE acquired for the N-CQD-7/*meso*-WO$_3$ in our work was the highest recorded value for WO$_3$ photoanodes decorated with carbon-based nanomaterials operating under similar conditions.

The influence of the direct annealing in air at 450 °C or in two-step annealing at 350 °C in N$_2$ then at 450 °C in the air on the *meso*-WO$_3$ photoanode PEC performance were investigated. Figure 8c shows the chopped LSVs at 50 mV·s^{-1} of *meso*-WO$_3$ annealed under different conditions in a 0.5 M Na$_2$SO$_4$ solution and under pulsed light irradiation. Clearly, as shown in Figure 8c, the *meso*-WO$_3$ photoanode annealed in two steps, firstly in N$_2$ then in air exhibits an oxygen evolution potential onset potential that was approximately 100 mV lower under light illumination, as well as a higher photocurrent density of up to 0.68 mA·cm^{-2} at 1.23 V vs. RHE, which was nearly two times greater than that of the WO$_3$ photoanode treated directly in air at 450 °C. This can be explained by the fact that annealing the WO$_3$ in an N$_2$ atmosphere first maintained the *meso*porous nature of WO$_3$ due to the presence of the residual carbon after burning the surfactant, leading to a high surface area and more active sites, and thus higher PEC performance. On the other hand, direct annealing in air destroyed the *meso*porous WO$_3$ framework, as confirmed by the SEM results in Figure 2c.

The corresponding applied bias photon-to-current efficiency (ABPE) of the *meso*-WO$_3$, and N-CQD-7/*meso*-WO$_3$ photoanodes under AM 1.5G illumination were estimated from the I–V curves via Equation (2).

$$\text{ABPE (\%)} = \left(\frac{[I \times [1.23\,v - V_b\,]]}{P_{tot}} \right) \times 100\% \tag{2}$$

where I = photocurrent density at applied bias V_b (mA/cm^2), V_b = applied bias (V), and P_{tot} = power density of the incident light (AM 1.5G, 100 mW·cm^{-2}). In particular, the efficiency of the *meso*-WO$_3$ photoelectrode at 1.0 V vs. RHE increased from 0.07% to 0.16% when the N-CQDs were incorporated into the *meso*porous structure. As mentioned earlier, the prolonged charge separation and transfer process of N-CQDs are the vital features for the promoted PEC behaviors of N-CQD/*meso*-WO$_3$ photoanode.

To obtain a better realization of the interfacial charge transfer behavior in the *meso*porous modified WO$_3$ photoanodes, an analysis of their EIS was performed. Figure 9a displays the Nyquist plots of the bare *meso*-WO$_3$ and N-CQD-7/*meso*-WO$_3$ electrodes at 1.23 V vs. RHE in the dark and under irradiation conditions.

The arc radius in the Nyquist plots indicates the charge transfer resistance at the electrode/electrolyte interface. The arc radius of the N-CQD-7/*meso*-WO$_3$ electrode under both dark and light conditions was clearly smaller than those in the corresponding pristine *meso*-WO$_3$ spectra, indicating faster interfacial charge transfer across the interface between the electrode and electrolyte and resulting in higher PEC performance [33,34,50]. In addition, the observed results evidenced that the N-doped CQDs increased the separation of charges (electrons and holes) in the N-CQD/*meso*-WO$_3$ electrode, and thus contributed to its higher PEC activity. Figure 9b displays the Mott−Schottky (M-S) plots of the N-CQD/*meso*-WO$_3$ and bare *meso*-WO$_3$ electrodes. A positive slope was observed in the M–S plots of bare *meso*-WO$_3$ and N-CQD-7/*meso*-WO$_3$, as expected for n-type semiconductors. The M-S curves clearly demonstrated that the N-CQD-7/*meso*-WO$_3$ electrode had a smaller slope than the pure *meso*-WO$_3$ sample, indicating the increased donor density and conductivity of the former.
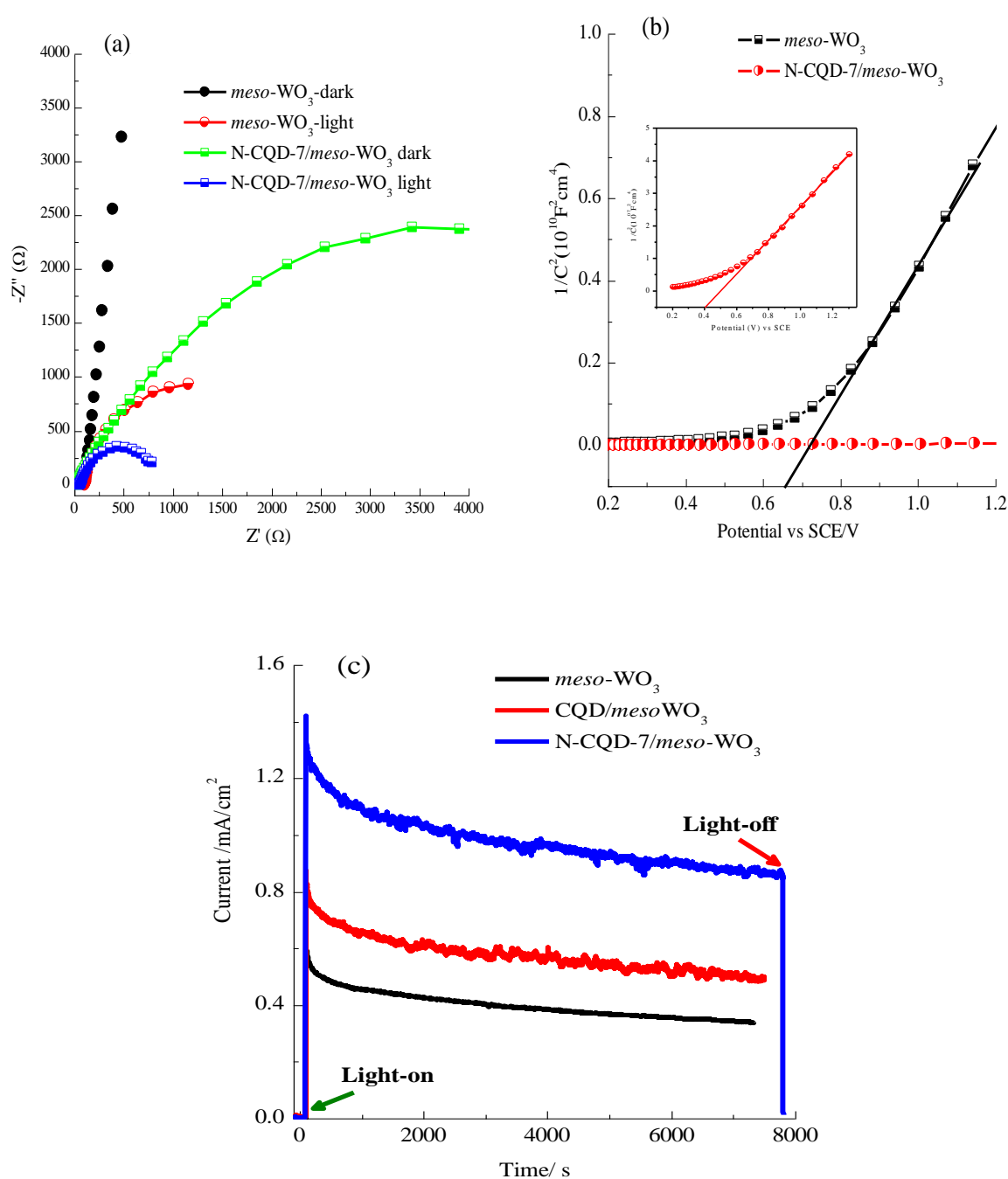
Figure 9. (**a**) Electrochemical impedance spectra (EIS) Nyquist-plots of pure *meso*-WO$_3$ and 7-N-CQDs/*meso*-WO$_3$ in the dark and under the irradiation conditions of AM 1.5G at a bias potential of 1.0 V vs. SCE with an AC voltage amplitude of 20 mV; (**b**) Mott–Schottky plots of the bare *meso*-WO$_3$ and N-CQDs/*meso*-WO$_3$ with a frequency of 1000 Hz in the dark and amplitude of 20 mV, (potential range 0.2–1.3 V); and (**c**) current-time curve of the *meso*-WO$_3$, CQDs/*meso*-WO$_3$, and 7-N-CQDs/*meso*-WO$_3$ composite electrode at an applied bias of 0.6 V vs. SCE under the illumination of AM 1.5G in 0.5M Na$_2$SO$_4$ solution (pH 6.8), light intensity 100 mW/cm^2.

The donor density of the pristine *meso*-WO$_3$ and N-CQD/*meso*-WO$_3$ electrode were estimated from the slopes of the M-S curves. The calculated donor density of N-CQD-7/*meso*-WO$_3$ was 2.30×1021 cm^{-3}, which was higher than that of pristine *meso*-WO$_3$ (4.01×1019 cm^{-3}). The improved donor density was credited to the presence of nitrogen in N-CQD, which reduced the charge recombination of hole-electron pairs and was thus credited to the superior photocurrent behavior of the N-CQD-7/*meso*-WO$_3$

photoanode. Furthermore, by extrapolating the linear M-S curve to the potential axis as presented in Figure 9b, the flat band potential (V_{FB}) of the pure *meso*-WO$_3$ and N-CQD/*meso*-WO$_3$ electrodes were estimated to be 0.658 and 0.405 V vs. SCE, correspondingly. The V_{FB} of N-CQD/*meso*-WO$_3$ was more negatively shifted and smaller than that of pure *meso*-WO$_3$, which matched the cathodic shift of the oxygen evolution reaction overpotential. The obvious negative shift of V_{FB} in N-CQD/*meso*-WO$_3$ enhanced the band bending at the interface of the N-CQD/*meso*-WO$_3$ and electrolyte, thereby decreasing the recombination of the photoinduced charge-carriers and the overpotential in the oxygen evolution reaction (OER) kinetics of the N-CQD/*meso*-WO$_3$ photoelectrode [51].

Finally, the durability of the *meso*-WO$_3$, CQD/*meso*-WO$_3$, and N-CQD-7/*meso*-WO$_3$ photoanodes was investigated using chronoamperometry in an 0.5 M Na$_2$SO$_4$ solution at an applied voltage of 0.6 V vs. SCE under AM 1.5G illumination, as displayed in Figure 9c. The photocurrent-time profile of N-CQD-7/*meso*-WO$_3$ exhibited better stability than that of bare *meso*-WO$_3$, with 65.6% of its initial performance being maintained (0.88 vs. 1.34 mA·cm^{-2}) after 2 h of testing. This demonstrated the role of the N-CQDs in improving the stability of the *meso*-WO$_3$ by reducing the charge-carrier recombination process or by the rapid and complete OER reaction [52,53].

Figure 10 shows a proposed PEC water-splitting mechanism for the enhanced performance of the present N-CQD-7/*meso*-WO$_3$ photoanodes. According to molecular orbitals (MOs) theory, various electronic transitions in N-CQD can be triggered the HOMO-LUMO (highest occupied molecular orbital, lowest unoccupied molecular orbital) energy levels under excitation of visible light [38,54], which results in a beneficial energy gap. Based on the linear potential scan method, the HOMO and LUMO positions of the N-CQD were assessed to be ≈ -0.27 and 2.14 eV (Figure 10), correspondingly. Moreover, the bandgap energy of N-CQDs of the electron transition obtained from the potential scans was 2.41 eV, which is consistent with earlier reports [55]. Besides, on the basis of Butler and Ginley's method, [56] the VB and CB energy levels of *meso*-WO$_3$ were assessed to be 0.74 and 3.44 eV vs. RHE, respectively. In addition, considering that the HUMO potential of N-CQDs was more positive than its corresponding VB potential of *meso*-WO$_3$, the photoexcited holes from VB of *meso*-WO$_3$ can instinctively transfer to the HUMO of N-CQDs. Simultaneously, the photoexcited electrons can also be transferred from N-CQDs to *meso*-WO$_3$. Hence, photoexcited electrons-holes were efficiently separated and the lifetime of the charge carriers was considerably continued. Lastly, the prolonging charge-carrier separation and transfer process can be credited to the enriched PEC response as argued earlier.
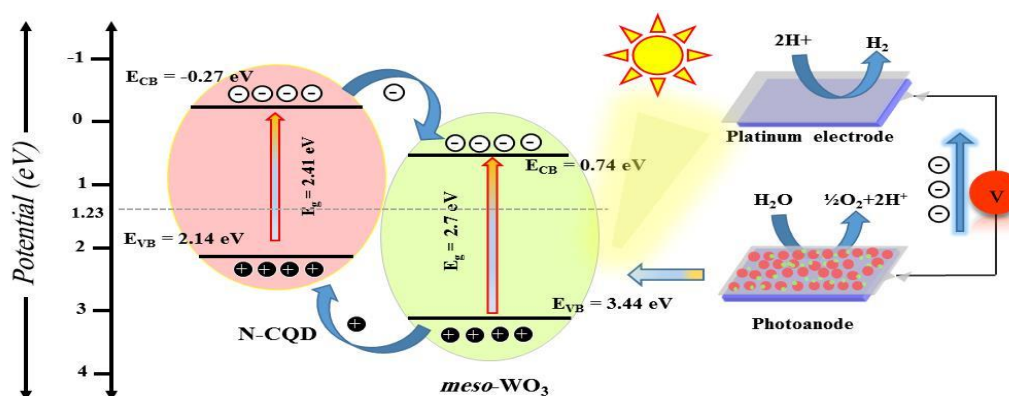
Figure 10. Proposed schematic energy-level diagram and charge migration process of N-CQDs/*meso*-WO$_3$ system for the photo-electrochemical (PEC) water oxidation.

4. Conclusions

In summary, we productively synthesized a tungsten trioxide WO$_3$ *meso*porous electrode via surfactant self-assembly and dip-coating methodologies using a high molecular-weight PEO-b-PS copolymer as a structure-directing template. This was followed by the incorporation of N-CQDs within the ordered *meso*structure through impregnation assembly. Importantly, the resulting

N-CQD/*meso*-WO$_3$ nanocomposites revealed considerably promoted PEC performance, with greater photocurrent densities (1.45 mA·cm^{-2} at 1.23 V vs. RHE) and low onset potentials (negatively shifted by 94 mV) compared to those of pristine *meso*-WO$_3$. Furthermore, the N-CQD/*meso*-WO$_3$ photoanode demonstrated a high ABPE of 0.16% at 1.0V vs. RHE. These results highlighted the multifunctional role of the hybridization of *meso*porous WO$_3$ with N-doped CQDs in the enhancement of PEC solar water splitting.

Supplementary Materials: The following are available online at http://www.mdpi.com/2079-4991/9/10/1502/s1, Figure S1: FTIR spectra of CQDs and N-CQDs samples, Figure S2: (a) XPS survey spectra for the CQDs, N-CQD-7 and N-CQD-20 samples. The only elements identified were carbon, nitrogen, and oxygen. (c) C 1s, (d) N 1s and (E) O 1s high resolution XPS spectra for N-CQD-7 sample, Figure S3: EDX spectra of N-CQDs samples, (a) N-CQD-3, (b) N-CQD-5, (c) N-CQD-7, and (d) N-CQD-20, Figure S4: (a) UV-Vis absorption spectra for the CQDs and N-CQDs samples. Inserts show digital photos of aqueous N-CQD-7 (left) and their bright blue PL (right) under UV, (b,c,d) PL spectra for the N-CQD-7, N-CQD−13, and N-CQD-20. The excitation wavelength was increased from 340 to 540 nm in 20 nm increments. (e) EQYs for the N-CQDs samples under 360 nm excitation, calibrated against quinine sulfate, Figure S5: steps for the synthesis of *meso*-WO$_3$ and modification with CQDs, Figure S6: Thickness of *meso*-WO$_3$ and modification with CQDs as measured by a profilometer, Table S1: a comparison the photocurrent density of WO$_3$ based composite materials.

Author Contributions: M.S.A. executed the experimental part and prepared the original draft; P.A. performed and analyzes the ISE part; S.P. executed the experimental part of the carbon quantum dots characterizations, analyze and wrote the results part; M.N.A. performed the XPS analysis part and A.M.A.-M. provided the fund, resources and supervises the overall research project. Finally, M.A.G. draws the conceptualization plan, analysis and validated the results, wrote, editing and submitted the manuscript in the final form.

Conflicts of Interest: The authors declare no conflict of interest.

References

1. Sivula, K.; Van De Krol, R. Semiconducting materials for photoelectrochemical energy conversion. *Nat. Rev. Mater.* **2016**, *1*, 15010. [CrossRef]

2. Seitz, L.C.; Chen, Z.; Forman, A.J.; Pinaud, B.A.; Benck, J.D.; Jaramillo, T.F. Modeling practical performance limits of photoelectrochemical water splitting based on the current state of materials research. *ChemSusChem* **2014**, *7*, 1372–1385. [CrossRef]

3. Cummings, C.Y.; Marken, F.; Peter, L.M.; Wijayantha, K.G.U.; Tahir, A.A. Study by Modulated Transmittance and Impedance Spectroscopies. *J. Am. Chem. Soc.* **2012**, *134*, 1228–1234. [CrossRef]

4. Wang, G.; Wang, H.; Ling, Y.; Tang, Y.; Yang, X.; Fitzmorris, R.C.; Wang, C.; Zhang, J.Z.; Li, Y. Hydrogen-treated TiO$_2$ nanowire arrays for photoelectrochemical water splitting. *Nano Lett.* **2011**, *11*, 3026–3033. [CrossRef]

5. Yang, Q.; Wang, W.; Xu, S.; Wang, Z.L. Enhancing light emission of ZnO microwire-based diodes by piezo-phototronic effect. *Nano Lett.* **2011**, *11*, 4012–4017. [CrossRef]

6. Kim, T.W.; Ping, Y.; Galli, G.A.; Choi, K.S. Simultaneous enhancements in photon absorption and charge transport of bismuth vanadate photoanodes for solar water splitting. *Nat. Commun.* **2015**, *6*, 8769. [CrossRef]

7. Kim, J.K.; Shin, K.; Cho, S.M.; Lee, T.W.; Park, J.H. Synthesis of transparent mesoporous tungsten trioxide films with enhanced photoelectrochemical response: Application to unassisted solar water splitting. *Energy Environ. Sci.* **2011**, *4*, 1465–1470. [CrossRef]

8. Chandra, D.; Saito, K.; Yui, T.; Yagi, M. Crystallization of tungsten trioxide having small mesopores: Highly efficient photoanode for visible-light-driven water oxidation. *Angew. Chem. Int. Ed.* **2013**, *52*, 12606–12609. [CrossRef]

9. Hartmann, P.; Lee, D.K.; Smarsly, B.M.; Janek, J. Mesoporous TiO$_2$: Comparison of classical sol-gel and nanoparticle based photoelectrodes for the water splitting reaction. *ACS Nano* **2010**, *4*, 3147–3154. [CrossRef]

10. Santato, C.; Odziemkowski, M.; Ulmann, M.; Augustynski, J. Crystallographically oriented mesoporous WO$_3$ films: Synthesis, characterization, and applications. *J. Am. Chem. Soc.* **2001**, *123*, 10639–10649. [CrossRef]

11. Liu, Y.; Koep, E.; Liu, M. A highly sensitive and fast-responding SnO$_2$ sensor fabricated by combustion chemical vapor deposition. *Chem. Mater.* **2005**, *17*, 3997–4000. [CrossRef]

12. Liu, J.; Gao, Y.; Wu, X.; Jin, G.; Zhai, Z.; Liu, H. Inhomogeneous oxygen vacancy distribution in semiconductor gas sensors: Formation, migration and determination on gas sensing characteristics. *Sensors* **2017**, *17*, 1852. [CrossRef]

13. Tian, B.; Liu, X.; Solovyov, L.A.; Liu, Z.; Yang, H.; Zhang, Z.; Xie, S.; Zhang, F.; Tu, B.; Yu, C.; et al. Facile Synthesis and Characterization of Novel Mesoporous and Mesorelief Oxides with Gyroidal Structures. *J. Am. Chem. Soc.* **2004**, *126*, 865–875. [CrossRef]

14. Deng, X.; Chen, K.; Tüysüz, H. Protocol for the Nanocasting Method: Preparation of Ordered Mesoporous Metal Oxides. *Chem. Mater.* **2017**, *29*, 40–52. [CrossRef]

15. Jo, C.; Hwang, J.; Song, H.; Dao, A.H.; Kim, Y.T.; Lee, S.H.; Hong, S.W.; Yoon, S.; Lee, J. Block-copolymer-assisted one-pot synthesis of ordered mesoporous WO_3-x/carbon nanocomposites as high-rate-performance electrodes for pseudocapacitors. *Adv. Funct. Mater.* **2013**, *23*, 3747–3754. [CrossRef]

16. Yang, P.; Zhao, D.; Margolese, D.I.; Chmelka, B.F.; Stucky, G.D. Generalized syntheses of large-pore mesoporous metal oxides with semicrystalline frameworks. *Nature* **1998**, *396*, 152–155. [CrossRef]

17. Zhou, W.; Li, W.; Wang, J.Q.; Qu, Y.; Yang, Y.; Xie, Y.; Zhang, K.; Wang, L.; Fu, H.; Zhao, D. Ordered mesoporous black TiO2 as highly efficient hydrogen evolution photocatalyst. *J. Am. Chem. Soc.* **2014**, *136*, 9280–9283. [CrossRef]

18. Cheng, W.; Baudrin, E.; Dunn, B.; Zink, J.I. Synthesis and electrochromic properties of mesoporous tungsten oxide. *J. Mater. Chem.* **2001**, *11*, 92–97. [CrossRef]

19. Walcarius, A. Mesoporous materials and electrochemistry. *Chem. Soc. Rev.* **2013**, *42*, 4098–4140. [CrossRef]

20. Linares, N.; Silvestre-Albero, A.M.; Serrano, E.; Silvestre-Albero, J.; García-Martínez, J. Mesoporous materials for clean energy technologies. *Chem. Soc. Rev.* **2014**, *43*, 7681–7717. [CrossRef]

21. Ye, Y.; Jo, C.; Jeong, I.; Lee, J. Functional mesoporous materials for energy applications: Solar cells, fuel cells, and batteries. *Nanoscale* **2013**, *5*, 4584–4605. [CrossRef] [PubMed]

22. Wei, J.; Sun, Z.; Luo, W.; Li, Y.; Elzatahry, A.A.; Al-Enizi, A.M.; Deng, Y.; Zhao, D. New insight into the synthesis of large-pore ordered mesoporous materials. *J. Am. Chem. Soc.* **2017**, *139*, 1706–1713. [CrossRef] [PubMed]

23. Li, Y.; Luo, W.; Qin, N.; Dong, J.; Wei, J.; Li, W.; Feng, S.; Chen, J.; Xu, J.; Elzatahry, A.A.; et al. Highly ordered mesoporous tungsten oxides with a large pore size and crystalline framework for H_2S sensing. *Angew. Chem. Int. Ed.* **2014**, *53*, 9035–9040. [CrossRef] [PubMed]

24. Zhu, Y.; Zhao, Y.; Ma, J.; Cheng, X.; Xie, J.; Xu, P.; Liu, H.; Liu, H.; Zhang, H.; Wu, M.; et al. Mesoporous Tungsten Oxides with Crystalline Framework for Highly Sensitive and Selective Detection of Foodborne Pathogens. *J. Am. Chem. Soc.* **2017**, *139*, 10365–10373. [CrossRef] [PubMed]

25. Arunachalam, P.; Amer, M.S.; Ghanem, M.A.; Al-Mayouf, A.M.; Zhao, D. Activation effect of silver nanoparticles on the photoelectrochemical performance of mesoporous TiO_2 nanospheres photoanodes for water oxidation reaction. *Int. J. Hydrog. Energy* **2017**, *42*, 11346–11355. [CrossRef]

26. Hu, D.; Diao, P.; Xu, D.; Wu, Q. Gold/WO_3 nanocomposite photoanodes for plasmonic solar water splitting. *Nano Res.* **2016**, *9*, 1735–1751. [CrossRef]

27. Ghanem, M.A.; Arunachalam, P.; Amer, M.S.; Al-Mayouf, A.M. Mesoporous titanium dioxide photoanodes decorated with gold nanoparticles for boosting the photoelectrochemical alkali water oxidation. *Mater. Chem. Phys.* **2018**, *213*, 56–66. [CrossRef]

28. Zhang, L.J.; Li, S.; Liu, B.K.; Wang, D.J.; Xie, T.F. Highly efficient CdS/WO_3 photocatalysts: Z-scheme photocatalytic mechanism for their enhanced photocatalytic H2 evolution under visible light. *ACS Catal.* **2014**, *4*, 3724–3729. [CrossRef]

29. Wang, Y.; Tian, W.; Chen, L.; Cao, F.; Guo, J.; Li, L. Three-Dimensional WO_3 Nanoplate/Bi_2S_3 Nanorod Heterojunction as a Highly Efficient Photoanode for Improved Photoelectrochemical Water Splitting. *ACS Appl. Mater. Interfaces* **2017**, *9*, 40235–40243. [CrossRef]

30. Lee, Y.L.; Huang, B.M.; Chien, H.T. Highly efficient CdSe-sensitized TiO_2 photoelectrode for quantum-dot-sensitized solar cell applications. *Chem. Mater.* **2008**, *20*, 6903–6905. [CrossRef]

31. Nozik, A.J. Quantum Dot Solar Cells. *Phys. E Low Dimens. Syst. Nanostructures* **2002**, *14*, 115–120. [CrossRef]

32. Li, H.; He, X.; Kang, Z.; Huang, H.; Liu, Y.; Liu, J.; Lian, S.; Tsang, C.H.A.; Yang, X.; Lee, S.T. Water-soluble fluorescent carbon quantum dots and photocatalyst design. *Angew. Chem. Int. Ed.* **2010**, *49*, 4430–4434. [CrossRef] [PubMed]

33. Shi, W.; Lv, X.; Shen, Y. BiOI/WO₃ photoanode with enhanced photoelectrochemical water splitting activity. *Front. Optoelectron.* **2018**, *11*, 367–374. [CrossRef]

34. Zhao, Z.; Butburee, T.; Peerakiatkhajohn, P.; Lyu, M.; Wang, S.; Wang, L.; Zheng, H. Carbon Quantum Dots sensitized Vertical WO₃ Nanoplates with Enhanced Photoelectrochemical Properties. *ChemistrySelect* **2016**, *1*, 2772–2777. [CrossRef]

35. Miao, R.; Luo, Z.; Zhong, W.; Chen, S.Y.; Jiang, T.; Dutta, B.; Nasr, Y.; Zhang, Y.; Suib, S.L. Mesoporous TiO2 modified with carbon quantum dots as a high-performance visible light photocatalyst. *Appl. Catal. B Environ.* **2016**, *189*, 26–38. [CrossRef]

36. Sk, M.A.; Ananthanarayanan, A.; Huang, L.; Lim, K.H.; Chen, P. Revealing the tunable photoluminescence properties of graphene quantum dots. *J. Mater. Chem. C* **2014**, *2*, 6954–6960. [CrossRef]

37. Kong, B.; Tang, J.; Zhang, Y.; Jiang, T.; Gong, X.; Peng, C.; Wei, J.; Yang, J.; Wang, Y.; Wang, X.; et al. Incorporation of well-dispersed sub-5-nm graphitic pencil nanodots into ordered mesoporous frameworks. *Nat. Chem.* **2016**, *8*, 171–177. [CrossRef]

38. Yeh, T.F.; Teng, C.Y.; Chen, S.J.; Teng, H. Nitrogen-doped graphene oxide quantum dots as photocatalysts for overall water-splitting under visible light illumination. *Adv. Mater.* **2014**, *26*, 3297–3303. [CrossRef]

39. Arcudi, F.; Dordevic, L.; Prato, M. Synthesis, separation, and characterization of small and highly fluorescent nitrogen-doped carbon nanodots. *Angew. Chem. Int. Ed.* **2016**, *55*, 2107–2112. [CrossRef]

40. Silverstein, R.M.; Webster, F.X.; Kiemle, D.J.; Bryce, D.L. Infrared Spectroscopy. In *Spectrometric Identification of Organic Compounds*, 8th ed.; Wiley: Hoboken, NJ, USA, 2014; pp. 71–125.

41. Hsu, P.C.; Chang, H.T. Synthesis of high-quality carbon nanodots from hydrophilic compounds: Role of functional groups. *Chem. Commun.* **2012**, *48*, 3984–3986. [CrossRef]

42. Shi, R.; Li, Z.; Yu, H.; Shang, L.; Zhou, C.; Waterhouse, G.I.N.; Wu, L.Z.; Zhang, T. Effect of Nitrogen Doping Level on the Performance of N-Doped Carbon Quantum Dot/TiO₂ Composites for Photocatalytic Hydrogen Evolution. *ChemSusChem* **2017**, *10*, 4650–4656. [CrossRef] [PubMed]

43. Liu, S.; Tian, J.; Wang, L.; Zhang, Y.; Qin, X.; Luo, Y.; Asiri, A.M.; Al-Youbi, A.O.; Sun, X. Hydrothermal treatment of grass: A low-cost, green route to nitrogen-doped, carbon-rich, photoluminescent polymer nanodots as an effective fluorescent sensing platform for label-free detection of Cu(II) ions. *Adv. Mater.* **2012**, *24*, 2037–2041. [CrossRef] [PubMed]

44. Zhu, S.; Zhang, J.; Tang, S.; Qiao, C.; Wang, L.; Wang, H.; Liu, X.; Li, B.; Li, Y.; Yu, W.; et al. Surface chemistry routes to modulate the photoluminescence of graphene quantum dots: From fluorescence mechanism to up-conversion bioimaging applications. *Adv. Funct. Mater.* **2012**, *22*, 4732–4740. [CrossRef]

45. Long, B.; Huang, Y.; Li, H.; Zhao, F.; Rui, Z.; Liu, Z.; Tong, Y.; Ji, H. Carbon Dots Sensitized BiOI with Dominant {001} Facets for Superior Photocatalytic Performance. *Ind. Eng. Chem. Res.* **2015**, *54*, 12788–12794. [CrossRef]

46. Tang, C.; Liu, E.; Wan, J.; Hu, X.; Fan, J. Co₃O₄ nanoparticles decorated Ag₃PO₄ tetrapods as an efficient visible-light-driven heterojunction photocatalyst. *Appl. Catal. B Environ.* **2016**, *181*, 707–715. [CrossRef]

47. Wang, Y.; Zhang, X.; Liu, J.; Wang, Y.; Duan, D.; Fan, C. Facile regeneration and photocatalytic activity of CuO-modified silver bromide photocatalyst. *Mater. Sci. Semicond. Process.* **2015**, *40*, 613–620. [CrossRef]

48. Liu, Y.; Li, Q.; Gao, S.; Shang, J.K. Template-free solvothermal synthesis of WO₃/WO₃•H₂O hollow spheres and their enhanced photocatalytic activity from the mixture phase effect. *CrystEngComm* **2014**, *16*, 7493–7501. [CrossRef]

49. Hilliard, S.; Baldinozzi, G.; Friedrich, D.; Kressman, S.; Strub, H.; Artero, V.; Laberty-Robert, C. Mesoporous thin film WO₃ photoanode for photoelectrochemical water splitting: A sol-gel dip coating approach. Sustain. *Energy Fuels* **2017**, *1*, 145–153.

50. Ye, K.H.; Wang, Z.; Gu, J.; Xiao, S.; Yuan, Y.; Zhu, Y.; Zhang, Y.; Mai, W.; Yang, S. Carbon quantum dots as a visible light sensitizer to significantly increase the solar water splitting performance of bismuth vanadate photoanodes. *Energy Environ. Sci.* **2017**, *10*, 772–779. [CrossRef]

51. Zhong, D.K.; Sun, J.; Inumaru, H.; Gamelin, D.R. Solar Water Oxidation by Composite Catalyst / r -Fe₂O₃ Photoanodes. *J. Am. Chem. Soc.* **2009**, *131*, 6086–6087. [CrossRef]

52. Zhang, P.; Wang, T.; Chang, X.; Zhang, L.; Gong, J. Synergistic Cocatalytic Effect of Carbon Nanodots and Co₃O₄ Nanoclusters for the Photoelectrochemical Water Oxidation on Hematite. *Angew. Chem. Int. Ed.* **2016**, *55*, 5851–5855. [CrossRef] [PubMed]

53. Liu, J.; Liu, Y.; Liu, N.; Han, Y.; Zhang, X.; Huang, H.; Lifshitz, Y.; Lee, S.T.; Zhong, J.; Kang, Z. Metal-free efficient photocatalyst for stable visible water splitting via a two-electron pathway. *Science* **2015**, *347*, 970–974. [CrossRef] [PubMed]

54. Tang, L.; Ji, R.; Li, X.; Teng, K.S.; Lau, S.P. Energy-level structure of nitrogen-doped graphene quantum dots. *J. Mater. Chem. C* **2013**, *1*, 4908–4915. [CrossRef]

55. Kong, W.; Zhang, X.; Liu, S.; Zhou, Y.; Chang, B.; Zhang, S.; Fan, H.; Yang, B. N Doped Carbon Dot Modified WO_3 Nanoflakes for Efficient Photoelectrochemical Water Oxidation. *Adv. Mater. Interfaces* **2019**, *6*, 1801653. [CrossRef]

56. Butler, M.A.; Ginley, D.S. Prediction of Flat band Potentials at Semiconductor-Electrolyte Interfaces from Atomic Electronegativities. *J. Electrochem. Soc.* **1978**, *125*, 228–232. [CrossRef]